



The investigation of primary creep regeneration for 10%Cr martensitic steel: Unified constitutive modelling

X. Li^{a,b}, S.R. Holdsworth^a, E. Mazza^{a,b}, E. Hosseini^{a,*}

^a Empa, Swiss Federal Laboratories for Material Science and Technology, Überlandstrasse 129, CH-8600 Dübendorf, Switzerland

^b ETH Zürich, Institute for Mechanical Systems, Department of Mechanical and Process Engineering, 8092 Zürich, Switzerland

ARTICLE INFO

Keywords:

Viscoplastic constitutive model
Primary creep regeneration
Chaboche model
Stress-varying creep loading
10%Cr steel

ABSTRACT

An elastic-viscoplastic constitutive material model is developed for the representation of the creep response of a 10%Cr steel under cyclic loading conditions. It has been shown that the model is able to describe primary creep regeneration (PCR), i.e. the incidence of a period of high creep strain rate following a stress reversal. The developed model is a variant of the well-known Chaboche viscoplastic constitutive model, and employs a bi-term power-law equation to represent the stress-regime dependence of the viscoplastic strain rate response. Back stress and drag stress are used to describe the kinematic and isotropic hardening/softening behaviour of the material, respectively. The evolutions of back stress and drag stress consider contributions from strain hardening, dynamic softening, static recovery and cyclic hardening/softening.

The effectiveness of the developed model for describing the sensitivity of the PCR behaviour to different loading parameters (e.g. reverse-loading magnitude and duration) and to represent the effect of PCR activation on the overall strain accumulation behaviour of the material is discussed. Furthermore, the predictive capability of the model is demonstrated for describing the response of the material during two independent benchmark tests; a stress-varying creep and a low-cycle fatigue experiments.

1. Introduction

High-chromium steels are widely used for the fabrication of high-temperature components in power plants which often operate under cyclic creep loading conditions. A proper understanding of the alloys' creep deformation responses under such cyclic (stress-varying) loading conditions is essential for their safe design and operation. An important consideration for assessing the creep response of materials under stress-varying loading conditions is primary creep regeneration (PCR) [1–7]. For a material deforming in the secondary creep regime, a load reversal might clear the strain hardening memory and lead to the incidence of a period of high creep strain rate after the stress-transient, similar to primary creep strain accumulation, i.e. PCR. A number of studies in 1950s–1970s have investigated the PCR response of metals such as aluminium, lead and cadmium [2–4,8]. With the emergence of renewable energy sources, the operation condition of conventional fossil-fired plants is changing and many critical high-temperature turbo-machinery parts now operate under cyclic loading conditions. Therefore, investigation of the PCR response of complex engineering alloys such as the stainless steel 316 and 10%Cr steel recently gained attentions [1,7,9–11]. Recent experimental studies [1,9,10] systematically investigated the PCR

behaviour of these two high-temperature steels under various loading conditions. Experimental observations confirmed that a period of fast creep often occurs after stress-transients (i.e. PCR), which consequently leads to more significant overall strain accumulation, in comparison to that for the constant-load creep condition. The creep rate after the stress transients and the extent of PCR activation depend on the prior deformation history of the material as well as the characteristics of the stress-transient profiles and differ for different alloys [1,9,10]. As the accumulated creep strain is an important parameter in the life-time assessment of high-temperature components (e.g. for ductility exhaustion damage calculations [12–14]), a representative mathematical description of PCR is needed for the mechanical integrity assessment of high-temperature components operating under stress-varying loading conditions.

The need for consideration of the PCR phenomenon in the mechanical integrity assessment of high-temperature components operating under cyclic loading conditions has been highlighted in a few previous studies [11,15,16]. A number of studies [11,17] took a pragmatic-simple approach and assumed that the accumulation of a minimum of 0.01% reverse inelastic strain clears the previous strain hardening memory of the material and consequently leads to re-occurrence of the primary creep stage upon reloading (i.e. PCR). The experimental

* Corresponding author at: High Temperature Integrity Group (HTIG), EMPA, Swiss Federal Laboratories for Materials Science and Technology, Switzerland.
E-mail address: ehsan.hosseini@empa.ch (E. Hosseini).

List of symbols and terminology

| | |
|--|--|
| A_1, A_2, n_1, n_2 | Temperature-dependent material constants in Eq. (6) |
| C_p, γ_p, K_i | Temperature-dependent material constants in Eq. (8) |
| C', γ', K' | Temperature-dependent material constants in Eq. (9) |
| D | Drag stress in Eq. (4) |
| E | Elastic modulus |
| LCF | Low-cycle fatigue |
| n | Direction of the viscoplastic strain rate in Eq. (1) |
| PCR | Primary creep regeneration |
| t | Time |
| t_1 | Forward-constant stress duration before a stress-transient (Fig. 1) |
| t_2 | Reverse-loading duration before reloading (Fig. 1) |
| t_l | Time at the end of a stress-transient (Fig. 8) |
| t'_{cr} | Creep time after a stress-transient (Fig. 8) |
| X | Back stress tensor in Eq. (1) |
| X' | Deviatoric part of back stress tensor in Eq. (1) |
| ϵ | Strain |
| ϵ_f | Total strain magnitude after a stress-transient (Fig. 8) |
| ϵ'_{cr} | Creep strain after a stress-transient (Fig. 8) |
| $ \epsilon_{vp} $ | Viscoplastic strain magnitude in Eq. (10) |
| ϵ^{eq}_{vp} | Accumulated von mises viscoplastic strain in Eq. (1) |
| σ | Stress tensor in Eq. (1) |
| σ' | Deviatoric part of stress tensor in Eq. (1) |
| σ_f | Forward-stress magnitude (Fig. 1) |
| σ_r | Reverse-stress magnitude (Fig. 1) |
| $\sigma_{r,1}, \sigma_{r,2}, \sigma_{r,3}, \sigma_{r,4}, \sigma_{r,5}$ | Compressive stress levels applied during stress-transients (Table 1) |
| ϵ_{vp} | Viscoplastic strain tensor in Eq. (1) |
| σ^* | Stress-dependent quantity in Eq. (5) |
| σ_0 | Stress level corresponding to a change of deformation mechanism in Eq. (5) |
| $\gamma_{i,\infty}, \gamma_{i,0}, w_{i,p}$ | Temperature-dependent material constants in Eq. (10) |
| $\gamma'_{\infty}, \gamma'_{i,0}, w'$ | Temperature-dependent material constants in Eq. (11) |

observations from a set of dedicated stress-varying creep experiments designed for evaluation of the PCR response for two high-temperature steels [1,9,10] showed that such a simple assumption cannot realistically represent the PCR behaviour. For example, it was found that some reverse-loading conditions might only partially clear the previous strain hardening memory, and therefore results in partial PCR activation upon reloading. It was also experimentally observed that, for reverse-loading to larger stresses or for longer reverse-loading durations, the creep rate upon reloading might be even higher than that of the initial primary creep stage of the material. The ineffectiveness of a simple switch-type PCR consideration highlights the necessity for the development of a more sophisticated model to realistically describe the PCR phenomenon. Physically-based models, such as the dislocation-based crystal-plasticity approach, consider the interaction of dislocations and obstacles at each slip system of individual grains [16], and are capable of representing the various levels of PCR activation. However, the complexity and high

computational cost of such models limit their application to small domain simulations and preclude their employment for the assessment of real-size components.

This study presents a variant of the computationally-efficient Chaboche viscoplastic constitutive model, based on [18,19], for the representation of the PCR response of a 10%Cr steel under different loading conditions at 600 °C. A comprehensive stress-varying creep testing program was employed to calibrate the developed model, and show the capability of the model to reliably represent PCR for various loading conditions. After the calibration and to demonstrate the effectiveness of the developed model, it was employed to predict the response of the alloy during independent load-controlled and strain-controlled benchmark tests.

2. Experimental details

The investigated material in this study is a 10%Cr steel with a chemical composition of 9.8%Cr, 1.4%Mo, 0.6%Ni, 0.4%Mn, 0.2% V and 0.1%C, which is often used as a steam turbine rotor material and was previously evaluated under low-cycle fatigue (LCF) and creep-fatigue conditions in [11,20,21]. This section briefly presents the details of ten stress-varying and two constant-load creep tests for the alloy. Readers are referred to [10] for a more comprehensive description of the creep tests. The experimental observations from these twelve load-controlled tests were used to calibrate the model and determine its parameters. Furthermore, as described in the following, one additional load-controlled independent benchmark test was performed in this study, which in combination with experimental observations from a strain-controlled low-cycle fatigue test from [20] were used for evaluating the predictive capability of the developed model.

The creep tests (twelve tests from [10] + one benchmark test conducted in the present study) employed uniaxial cylindrical dog-bone bar specimens, with gauge diameter and length of 8 mm and 50 mm, respectively. The tests were carried out using a 100 kN servoelectromechanical Schenck universal testing machine in load-controlled mode. A closed-loop three-zone resistance furnace was used for heating the specimens to the test temperature of 600 ± 1 °C. Three thermocouples were attached along the specimen gauge length to monitor the temperature gradient and confirm it to be less than ± 1.5 °C within the specimen gauge length during the creep test. Two symmetrically arranged rod-tube type extensometers were employed to continuously measure the strain evolution, and an in-house developed Labview program was used for continuous data acquisition and recording of the strain, force, and temperature signals during the experiments.

The creep tests from [10] were designed to study the PCR behaviour and its sensitivity to different loading parameters. Fig. 1 shows an example of the examined loading profiles. Each test contained three segments, and each segment consisted of nine stress-transients. The nine different stress-transients in each segment enabled evaluation of the influence of different reverse-loading magnitude on PCR and the three segments in each test allowed investigation of the sensitivity of the PCR behaviour to the segment number (creep testing time and accumulated creep strain). As shown in Table 1, the experimental program included tests with three different reverse-loading durations (t_2) and four different forward-stress levels (σ_f), which aimed to assess the dependence of the PCR phenomenon on the reverse-stress duration and forward-stress level, respectively. Furthermore, two constant-load creep tests were performed to generate reference creep curves to be compared with those from stress-varying creep tests, and highlight the effect of stress-transients on the overall strain accumulation behaviour of the 10%Cr steel at 600 °C.

Fig. 2 illustrates the designed stress profile for the conducted benchmark test in the present study. The employed testing setup was the same as that developed in [10] and shortly described above. The benchmark test included different forward-loading levels, and different reverse-loading magnitudes and durations. The designed loading profile allowed

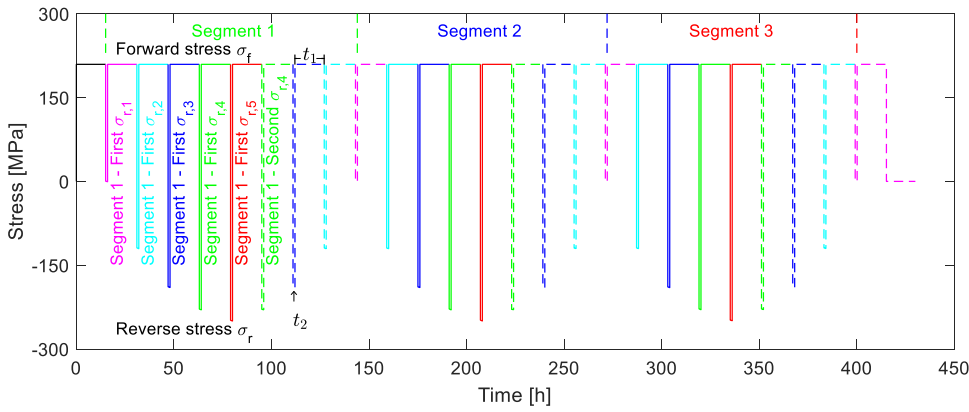


Fig. 1. An example of the transients applied during stress-varying creep tests (e.g. test 6). Different colours are used to represent stress-transients to different stress levels, e.g. the blue colour is used for reverse-loading to $\sigma_{r,3}$. Also solid and dashed lines are used to differentiate between the first and second stress-transients to the same stress magnitude in each segment [10].

Table 1

Details for the conducted stress-varying (#1–10) and constant-load (#11&12) creep tests for the 10%Cr steel. All tests were performed at 600 °C [10].

| Test # | Forward-stress [MPa] | t_1 [h] | t_2 [h] | $\sigma_{r,1}$ [MPa] | $\sigma_{r,2}$ [MPa] | $\sigma_{r,3}$ [MPa] | $\sigma_{r,4}$ [MPa] | $\sigma_{r,5}$ [MPa] |
|--------|----------------------|-----------|-----------|----------------------|----------------------|----------------------|----------------------|----------------------|
| 1 | 190 | 15 | 0 | 0 | –135 | –270 | –385 | –405 |
| 2 | 210 | 15 | 0 | 0 | –135 | –270 | –385 | –405 |
| 3 | 230 | 15 | 0 | 0 | –135 | –270 | –385 | –405 |
| 4 | 250 | 15 | 0 | 0 | –135 | –270 | –385 | –405 |
| 5 | 190 | 15 | 1 | 0 | –120 | –190 | –230 | –250 |
| 6 | 210 | 15 | 1 | 0 | –120 | –190 | –230 | –250 |
| 7 | 230 | 15 | 1 | 0 | –120 | –190 | –230 | –250 |
| 8 | 250 | 15 | 1 | 0 | –120 | –190 | –230 | –250 |
| 9 | 190 | 15 | 15 | 0 | –120 | –190 | –230 | –250 |
| 10 | 230 | 15 | 15 | 0 | –120 | –190 | –230 | –250 |
| 11 | 190 | 765 | – | – | – | – | – | – |
| 12 | 230 | 765 | – | – | – | – | – | – |

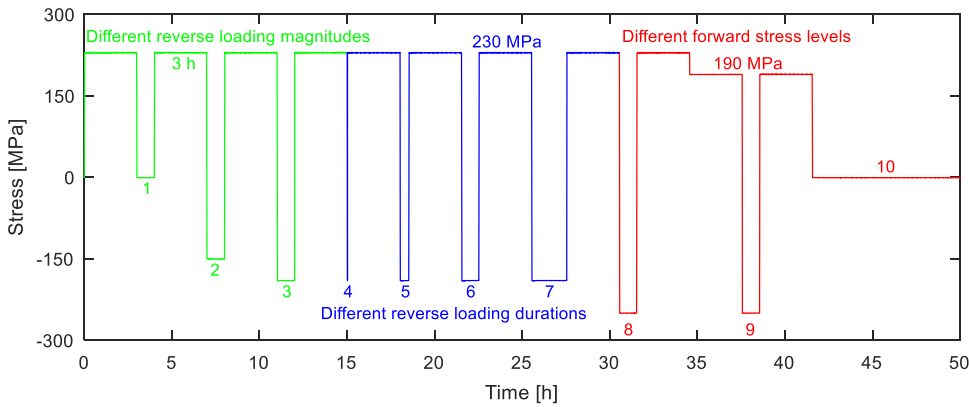


Fig. 2. Loading profile of the conducted benchmark test (transient #1: 0 MPa/1 h; #2: 150 MPa/1 h; #3: 190 MPa/1 h; #4: 190 MPa/0 h; #5: 190 MPa/0.5 h; #6: 190 MPa/1 h; #7: 190 MPa/2 h; #8: 250 MPa/1 h; #9: 250 MPa/1 h; #10: 0 MPa/8 h).

verification of the effectiveness of the developed model for predicting the creep behaviour of the material under a rather complex loading scenario.

3. MODEL description and calibration

Different variants of Chaboche unified viscoplastic constitutive models have been employed for representing the cyclic deformation response of different materials at ambient and elevated temperature conditions [18,22–35]. The Chaboche model defines the viscoplastic strain rate as:

$$\dot{\epsilon}_{vp} = \frac{3}{2} \dot{\epsilon}_{vp}^{eq} \frac{\sigma' - \mathbf{X}'}{\|\sigma - \mathbf{X}\|} = \dot{\epsilon}_{vp}^{eq} \mathbf{n} \quad (1)$$

$$\|\sigma - \mathbf{X}\| = \sqrt{\frac{3}{2} (\sigma' - \mathbf{X}') : (\sigma' - \mathbf{X}')} \quad (2)$$

$$\dot{\epsilon}_{vp}^{eq} = \sqrt{\frac{2}{3} \dot{\epsilon}_{vp}^{eq} : \dot{\epsilon}_{vp}^{eq}} \quad (3)$$

where σ and \mathbf{X} are the applied stress and back stress tensors respectively, and σ' and \mathbf{X}' are their deviatoric parts accordingly. A three-term backstress formulation $\mathbf{X} = \sum_{j=1}^3 \mathbf{X}_j$ is employed in this study (similar to [36–38]). The tensor \mathbf{n} defines the direction of the viscoplastic strain rate and $\dot{\epsilon}_{vp}^{eq}$ is the equivalent von Mises viscoplastic strain rate. Walker [24] proposed a power-law relationship for describing the dependency of equivalent viscoplastic strain rate on the stress state as:

$$\dot{\epsilon}_{vp}^{eq} = A \left(\frac{\|\sigma - \mathbf{X}\|}{D} \right)^n \quad (4)$$

where A , n are temperature-dependant material constants, and D is referred to as the drag stress. As the material deformation mechanism is

different in different stress-regimes [39,40], the simple Eq. (4) might fail to represent the response of materials over a wide range of stresses. A number of studies [41–44] therefore proposed the consideration of stress-regime dependent formulations, e.g.:

$$\dot{\epsilon}_{vp}^{eq} = \begin{cases} A_1 \sigma^{*n_1} & \sigma^* \geq \sigma_0 \\ A_2 \sigma^{*n_2} & \sigma^* < \sigma_0 \end{cases} \quad (5)$$

or

$$\dot{\epsilon}_{vp}^{eq} = A_1 \sigma^{*n_1} + A_2 \sigma^{*n_2} \quad (6)$$

where A_1 , A_2 , n_1 and n_2 are temperature-dependent material constants, σ^* is a stress-dependent quantity, and σ_0 is the stress level corresponding to a change of deformation mechanism. In comparison to Eq. (5) which assumes a sudden change of deformation mechanism at the stress level of σ_0 , Eq. (6) represents a gradual change of the deformation mechanism. With consideration of the latter, Eq. (4) can be rewritten as:

$$\dot{\epsilon}_{vp}^{eq} = \sum_{i=1}^2 A_i \left(\frac{\|\sigma - \mathbf{X}\|}{D} \right)^{n_i} \quad (7)$$

The kinematic hardening/softening parameter \mathbf{X} (back stress) in above equation describes the internal stress fields, while the isotropic hardening/softening parameter D (drag stress) represents the evolution of the material's isotropic resistance to the dislocation movement [16,27,45,46]. Following [18,23,47], the evolutions of back stress \mathbf{X} and drag stress D are defined as:

$$\dot{\mathbf{X}}_i = C_i \dot{\epsilon}_{vp} - \gamma_i \mathbf{X}_i \dot{\epsilon}_{vp}^{eq} - K_i \mathbf{X}_i, \quad \mathbf{X}_i|_{t=0} = 0 \quad (8)$$

$$\dot{D} = C' \dot{\epsilon}_{vp}^{eq} - \gamma' D \dot{\epsilon}_{vp}^{eq} - K' D, \quad D|_{t=0} = D_0 \quad (9)$$

where C_i , γ_i , K_i , C' , γ' and K' are temperature-dependent material constants. The three terms in Eqs. (8) and (9) represent contributions of strain hardening, dynamic softening and static recovery in material hardening/softening response, respectively. An extension of the Armstrong-Fredrick formulation was proposed by Seifert and Metzger [19,48,49] to represent materials cyclic hardening/softening by considering γ parameters dependent on the viscoplastic strain quantities. Following their work, this study considered that γ_i and γ' in Eqs. (8) and (9) are dependent on the viscoplastic strain magnitude $\|\epsilon_{vp}\|$ and accumulated viscoplastic strain $\epsilon_{vp}^{eq} = \int \dot{\epsilon}_{vp}^{eq} dt$, respectively:

$$\gamma_i = \gamma_{i,\infty} + (\gamma_{i,0} - \gamma_{i,\infty}) \exp(-w_i \|\epsilon_{vp}\|) \quad (10)$$

$$\gamma' = \gamma'_{\infty} + (\gamma'_{0} - \gamma'_{\infty}) \exp(-w' \epsilon_{vp}^{eq}) \quad (11)$$

where $\gamma_{i,\infty}$, $\gamma_{i,0}$, w_i , γ'_{∞} , γ'_{0} , and w' are temperature-dependent material constants.

As the investigated data in this study are from uniaxial experiments, the 1D representation of the developed model was derived as follows.

$$\dot{\sigma} = E(\dot{\epsilon} - \dot{\epsilon}_{vp}) \quad (12)$$

$$\dot{\epsilon}_{vp} = \sum_{i=1}^2 A_i \left(\frac{|\sigma - X|}{D} \right)^{n_i} \text{sign}(\sigma - X) \quad (13)$$

$$\dot{X}_i = C_i \dot{\epsilon}_{vp} - \gamma_i X_i \dot{\epsilon}_{vp}^{eq} - K_i X_i \quad (14)$$

$$\gamma_i = \gamma_{i,\infty} + (\gamma_{i,0} - \gamma_{i,\infty}) \exp(-w_i |\epsilon_{vp}|) \quad (15)$$

$$\dot{D} = C' \dot{\epsilon}_{vp}^{eq} - \gamma' D \dot{\epsilon}_{vp}^{eq} - K' D \quad (16)$$

$$\gamma' = \gamma'_{\infty} + (\gamma'_{0} - \gamma'_{\infty}) \exp(-w' \epsilon_{vp}^{eq}) \quad (17)$$

Calibration of the model for representing the deformation behaviour of 10%Cr steel at 600 °C employed the experimental records from the

twelve load-controlled creep tests. The calibration was based on solving an optimization problem which aims to find a set of model parameters whose employment in the model formulation results in the best possible representation of the available experimental data. Mathematically, the problem minimises the error formulation given below by optimization of the material model parameters.

$$\text{error} = \sum_{i=1}^{12} \left[\sum_{j=1}^{N_i} \left(\epsilon_{\text{experiment},i}^j - \epsilon_{\text{model},i}^j \right)^2 / \sum_{j=1}^{N_i} \left(\epsilon_{\text{experiment},i}^j \right)^2 \right] \quad (18)$$

where $\epsilon_{\text{experiment},i}^j$ and $\epsilon_{\text{model},i}^j$ are experimentally measured and model calculated strains for time-frame j of creep test i , and N_i is the total number of time frames for the creep test i .

This study used the global search function of the MATLAB® optimization toolbox for solving the optimization problem. The derived set of model parameters for the 10%Cr steel at 600 °C are given in Table 2. Section 4 presents the comparison between model results and measurements. Section Supplementary Material provides a MATLAB® code which uses the derived model parameters for calculation of the strain response of the material for a given stress profile.

As an example, Fig. 3 presents the model calculated viscoplastic strain, drag stress and back stress for the given stress profile in Fig. 3a. The stress profile includes 3 different stress-transients which result in different extents of PCR upon reloading (Fig. 3b). Fig. 3c presents a global reduction of the drag stress which is consistent with the well-known softening response of martensitic steels. The back stress evolution in Fig. 3d shows that the back stress plays an important role in defining the extent of PCR activation after the stress-transients. It can be seen that the back stress decreases only slightly during the first unloading to 0 MPa, and leads to insignificant PCR upon reloading. Reverse-loading to -120 MPa reduces the back stress from ~40 MPa to a value close to 20 MPa, and results in partial PCR upon reloading. Significant PCR is achieved after stress-transient to -190 MPa which reduces the back stress to a negative value before reloading.

4. Model results and discussions

Comparison of experimental and model calculated strain evolutions for the creep tests are shown in Fig. 4 ($t_2 = 0$ h, tests 1–4), Fig. 5 ($t_2 = 1$ h, tests 5–8), Fig. 6 ($t_2 = 15$ h, tests 9–10) and Fig. 7 (constant-load creep, tests 11–12). It can be observed that the developed model well describes the creep behaviours of the alloy under various loading conditions. The model representations are qualitatively-consistent with the observations from the twelve experiments, although discrepancies between the experimental and model-predicted strain profiles are acknowledged. The inconsistencies mainly originate from the complex nature of the examined loading profiles which challenge any type of material constitutive model for providing a quantitatively accurate representation. Nevertheless and as discussed in Sections 4.1 and 4.2, the model is able to present a reliable description for the sensitivity of the PCR phenomenon and the overall strain accumulation response of the alloy to different parameters of loading profiles. The predictive capabilities of the model are analyzed in Section 4.3 where the equations are used for describing the creep behaviour of the alloy during two independent benchmark tests: one load-controlled experiment performed in the present study (Fig. 2) and one strain-controlled low-cycle fatigue test reported in [20].

4.1. Effect of loading parameters on the extent of PCR

This section examines the effectiveness of the developed model for describing the influence of different loading parameters on the PCR behaviour of 10%Cr steel at 600 °C. In addition, the evolutions of back stress and drag stress under different loading conditions are discussed. This is because the creep strain rates upon reloading, i.e. the extent of PCR, are determined by the evolutions of back stress and drag stress

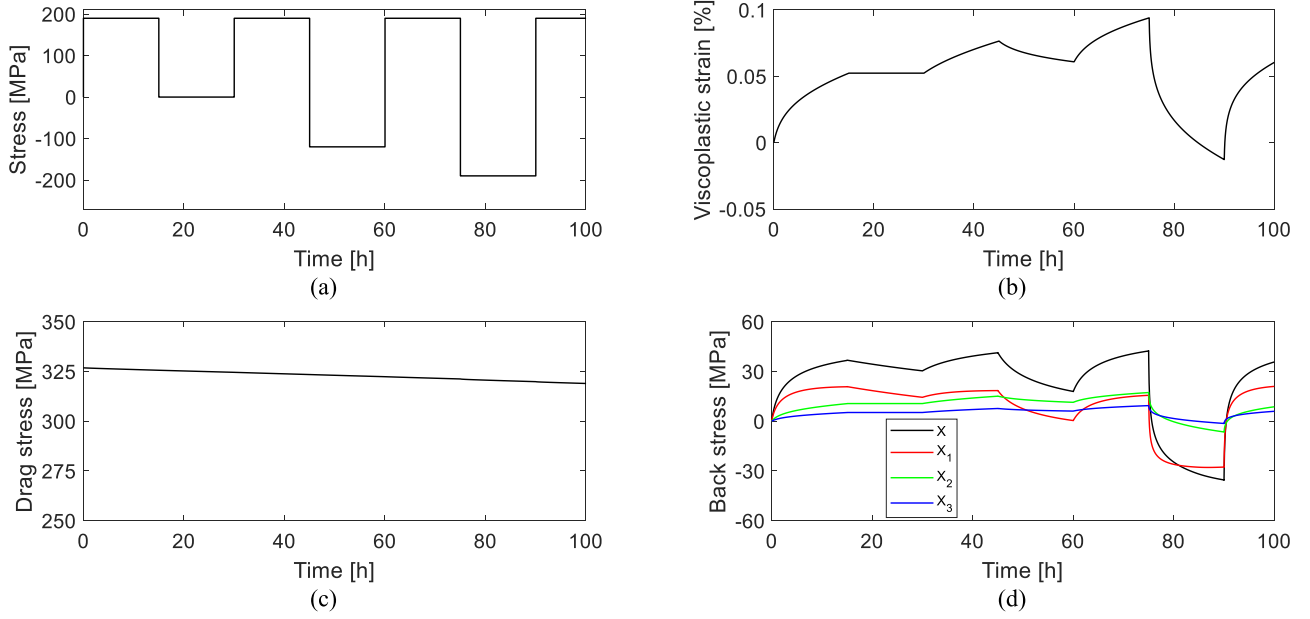


Fig. 3. Representation of the developed model for a given stress profile (a) in terms of viscoplastic strain (b), drag stress (c) and back stress (d). Back stress X in (d) is the summation of three back stress terms X_1 , X_2 and X_3 . The model represents different extents of PCR activation depending on the level of reverse-loading.

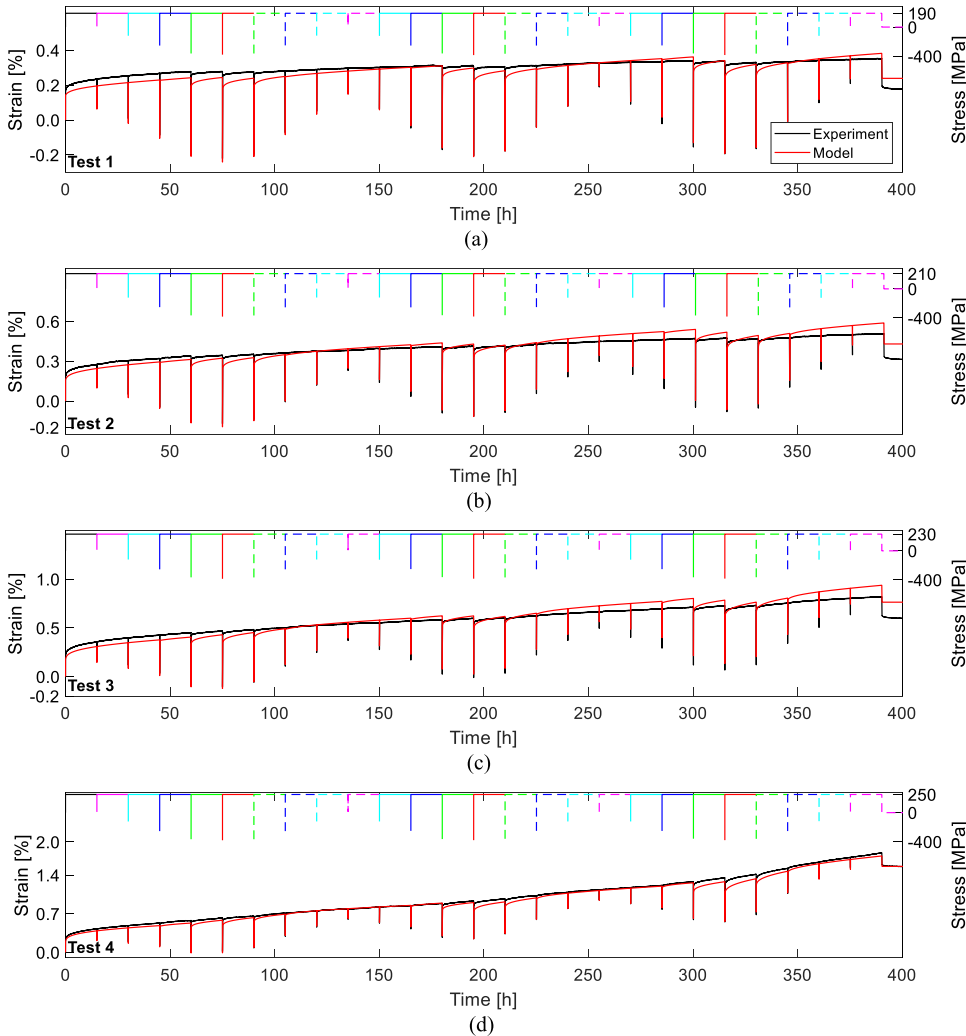


Fig. 4. Comparison of the model represented strain profiles with the experimental observations under stress-varying creep tests with $t_2 = 0$ h at 600 °C (tests 1–4). Experimental data are taken from [10].

Table 2
Obtained model parameters for the 10%Cr steel at 600 °C.

| Parameter | Value | Unit | Parameter | Value | Unit | Parameter | Value | Unit |
|----------------|------------------------|------|---------------------|-----------------------|------|---------------------|-----------------------|------|
| E | 1.32×10^2 | GPa | γ'_{∞} | 3.75×10^0 | – | $\gamma_{2,0}$ | 9.52×10^1 | – |
| D ₀ | 3.27×10^2 | MPa | w' | 7.73×10^{-1} | – | $\gamma_{2,\infty}$ | 1.11×10^3 | – |
| A ₁ | 1.41×10^{-1} | 1/s | C ₁ | 8.20×10^4 | MPa | w ₂ | 1.74×10^2 | – |
| n ₁ | 1.21×10^1 | – | K ₁ | 2.46×10^{-2} | 1/s | C ₃ | 1.01×10^4 | MPa |
| A ₂ | 1.46×10^{-18} | 1/s | $\gamma_{1,0}$ | 1.87×10^3 | – | K ₃ | 5.66×10^{-6} | 1/s |
| n ₂ | 2.78×10^2 | – | $\gamma_{1,\infty}$ | 2.27×10^3 | – | $\gamma_{3,0}$ | 6.73×10^{-1} | – |
| C' | 7.58×10^2 | MPa | w ₁ | 3.76×10^3 | – | $\gamma_{3,\infty}$ | 2.87×10^2 | – |
| K' | 2.13×10^{-4} | 1/s | C ₂ | 2.12×10^4 | MPa | w ₃ | 3.09×10^1 | – |
| γ'_0 | 3.36×10^0 | – | K ₂ | 6.10×10^{-6} | 1/s | | | |

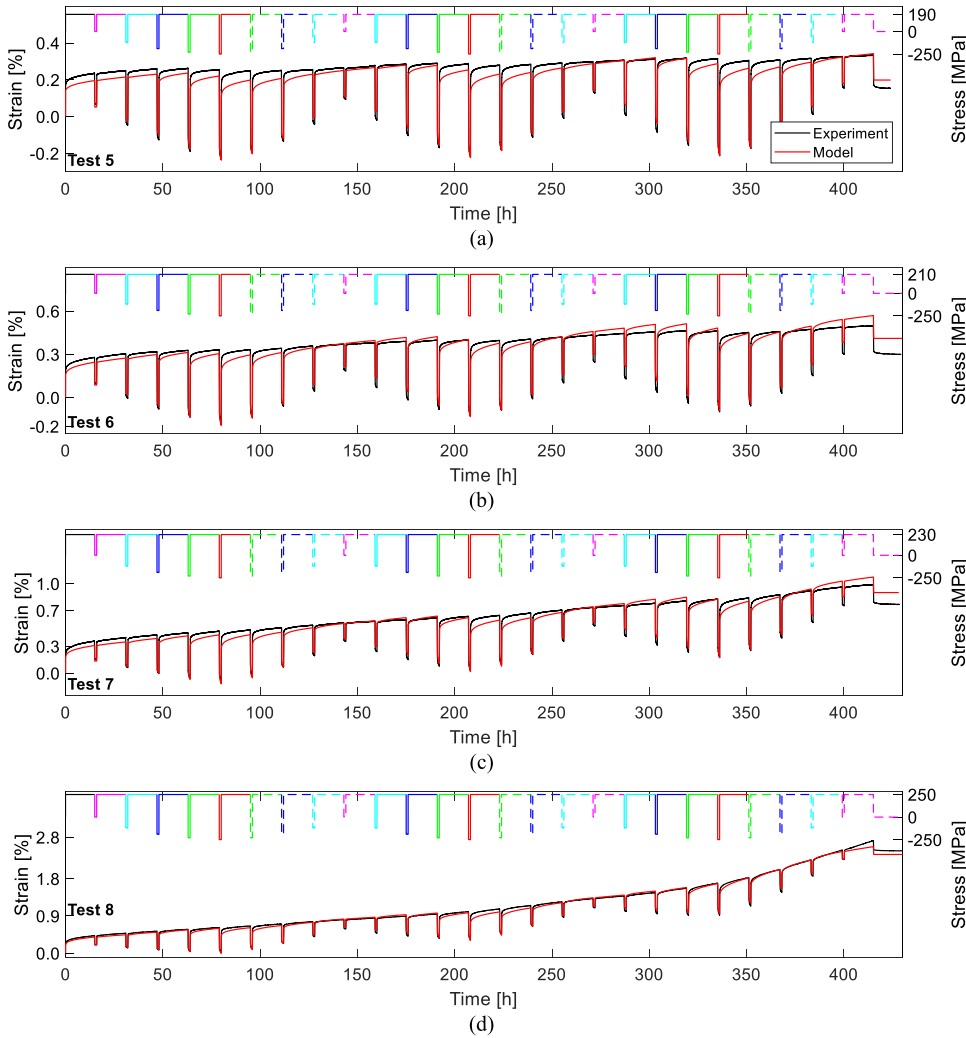


Fig. 5. Comparison of the model represented strain profiles with the experimental observations under stress-varying creep tests with $t_2 = 1$ h at 600 °C (tests 5–8). Experimental data are taken from [10].

during the stress-transients. Eq. (4) shows that the decrease in back stress (and drag stress) during the reverse-loading can lead to high creep strain rates upon reloading (i.e. PCR). Different loading parameters (e.g. reverse-loading magnitude and duration) can affect the back stress (and drag stress) evolutions during the stress-transients, and therefore result in different levels of PCR activation upon reloading.

Two parameters of creep strain (ϵ'_{cr}) and creep time (t'_{cr}) are introduced in Fig. 8a to investigate the PCR behaviour under stress-varying loading conditions. The comparison of ϵ'_{cr} as a function of t'_{cr} after various stress-transients with that for the as-received alloy (i.e. the creep strain evolution during the first 15 h of each test) allows an estimation of the extent of PCR after the stress-transients and therefore enables the investigation of the PCR sensitivity to the different loading parameters. Fig. 8b represents an example of partial activation of PCR, where high

creep strain rates after the stress-transient are clearly observed, but the extent of creep strain accumulation after the stress-transient is smaller than that for the as-received material.

4.1.1. Effect of reverse-loading magnitude

Fig. 9 compares the experimental and model representations of the creep response of the alloy after transients to different reverse-loading magnitudes. Consistent with the experimental records in Fig. 9a and b, more significant PCR activation after stress-transients to larger reverse-loading magnitudes are given by the model (Fig. 9c and d), which demonstrates its capability for the realistic representation of the sensitivity of the PCR behaviour to the reverse-loading scale. The model gives a generally representative description of the experimental records, although quantitative inconsistencies, for example, of the as-received

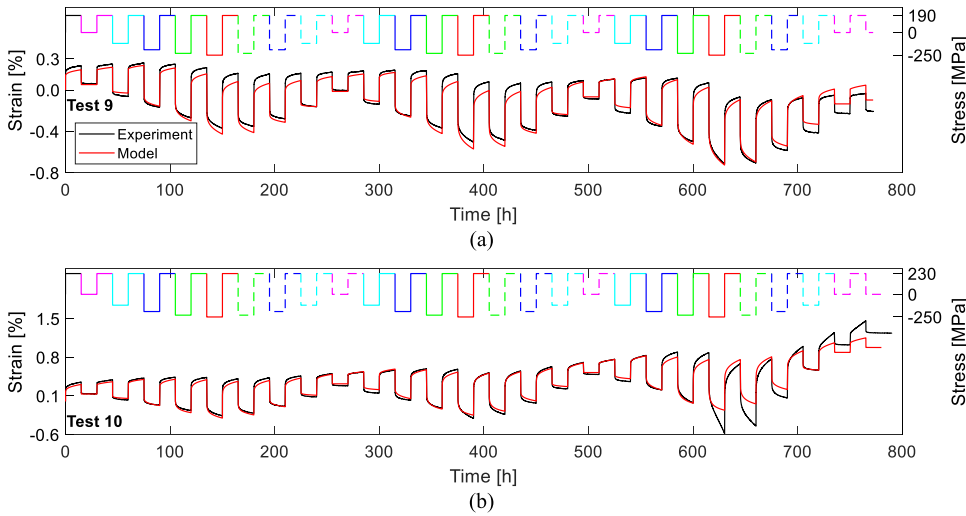


Fig. 6. Comparison of the model represented strain profiles with the experimental observations under stress-varying creep tests with $t_2 = 15$ h at 600 °C (tests 9–10). Experimental data are taken from [10].

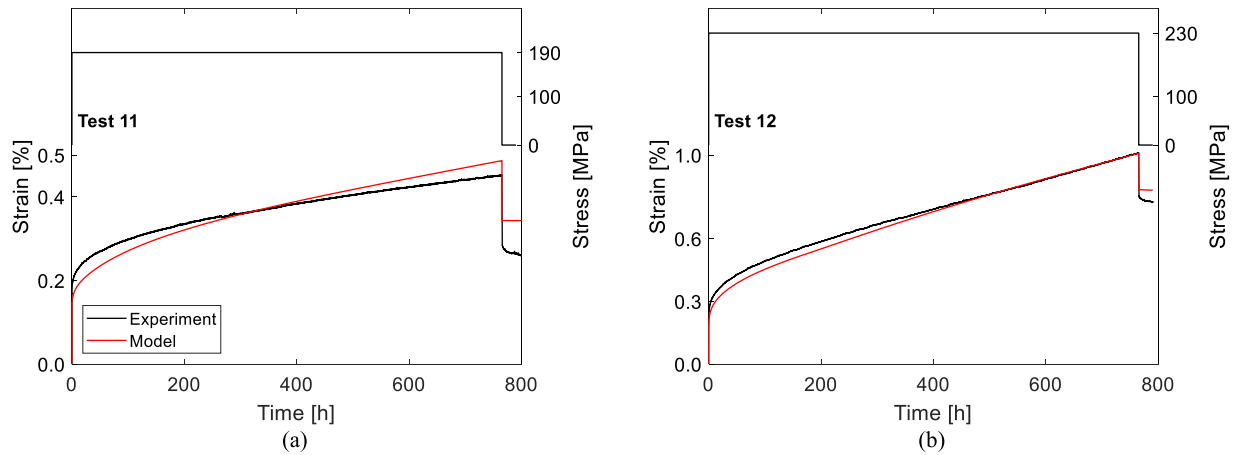


Fig. 7. Comparison of the model represented strain profiles with the experimental observations under constant-load creep tests at 600 °C (tests 11–12). Experimental data are taken from [10].

alloy's creep response in Fig. 9, are visible. Fig. 10b and c present the model calculated evolutions of back stress and drag stress during the given stress profile in Fig. 10a. It can be seen that stress-transients to larger reverse-loading magnitudes result in lower back stresses at the end of the compressive loading period, while the evolution of drag stress is not significantly sensitive to the reverse-loading level. Eq. (4) indicates that a smaller back stress after the stress-transient results in faster creep upon reloading. Therefore, the more pronounced decrease of back stress during reverse-loading to larger compressive stresses leads to a more significant PCR upon reloading.

4.1.2. Effect of reverse-loading duration

Experimental observations presented in Fig. 11a and b indicate a more significant PCR after longer reverse-loading durations. The figures show that, for the same forward- and reverse-loading magnitudes, 15 h reverse-loading causes a higher creep rate after reloading and therefore larger extents of PCR, when compared with the reverse-loading duration of 1 h. The modelling results presented in Fig. 11c and d demonstrate that the developed model can consistently represent the sensitivity of the PCR behaviour to the reverse-loading duration. Examination of the evolution of back stress and drag stress for stress-transients with 1 and 15 h reverse-loading in Fig. 12 explains that longer reverse-loading further reduces the back stress and, according to Eq. (4), results in a faster creep strain accumulation upon reloading and therefore more significant PCR. The effect of reverse-loading duration on the drag stress quantity

is rather marginal and is not expected to play the main role in defining the PCR sensitivity to the duration of reverse-loading.

4.1.3. Effect of segment number

The experimental records presented in Fig. 13a and b show that the extent of PCR is more significant for the larger segment numbers which correspond to longer creep testing times and larger accumulated creep deformation. This PCR behaviour is correctly represented by the developed model, as shown in Fig. 13c and d, which demonstrates the effectiveness of the model for describing the sensitivity of PCR to the segment number. Fig. 14 shows the evolutions of back stress and drag stress during the stress-transients to $\sigma_{r,4}$ in different segments of test 6. The smaller back stress and drag stress at the end of stress-transients explain the higher creep rates after reloading and therefore more pronounced PCR for larger segment numbers.

4.1.4. Effect of forward-stress magnitude

Fig. 15 shows the sensitivity of PCR activation to the forward-stress level of the conducted stress-varying creep tests. The presented experimental data in Fig. 15a–d indicates that the extent of PCR is more significant for smaller forward-stress levels. Fig. 15e–h show that this behaviour is well represented by the developed model. Fig. 16 shows the calculated evolutions of back stress and drag stress during the stress-transients to $\sigma_{r,5}$ in segment 1 of tests 5 and 7. As can be seen, the back stress at the end of a stress-transient is smaller for test 5 with the smaller

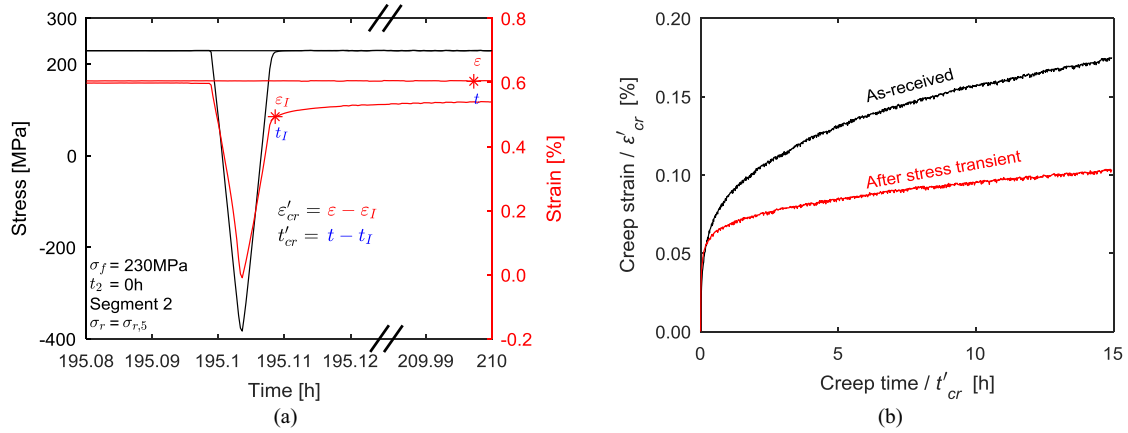


Fig. 8. Description of the methodology used for calculation of the creep strain ϵ'_{cr} and creep time t'_{cr} after a stress-transient (a), and comparison of creep strain evolution after a stress-transient with that for the as-received alloy (b). Two parameters ϵ_I and t_I are strain and time at the start of the constant-stress loading period, respectively [9,10].

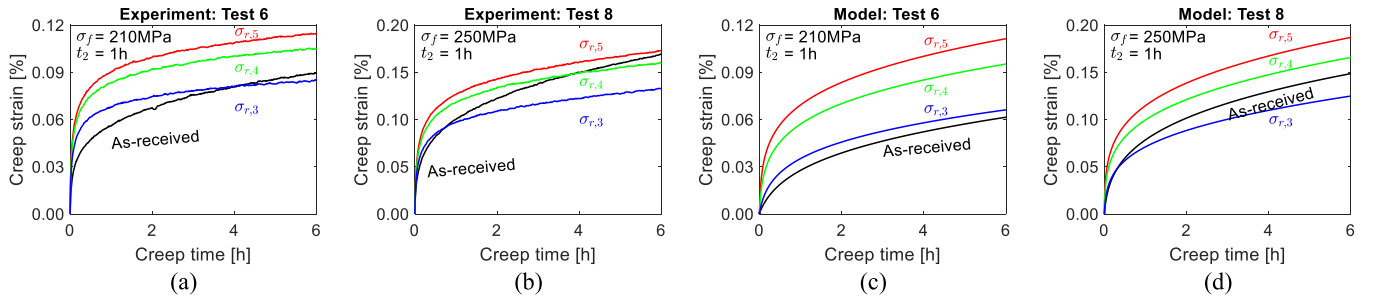


Fig. 9. Sensitivity of the PCR behaviour of the 10%Cr steel to the reverse-loading magnitude: experimental observations (a and b) and modelling results (c and d) for strain accumulation after reverse-loading to $\sigma_{r,3}$, $\sigma_{r,4}$ and $\sigma_{r,5}$ in tests 6 and 8 (segment 1).

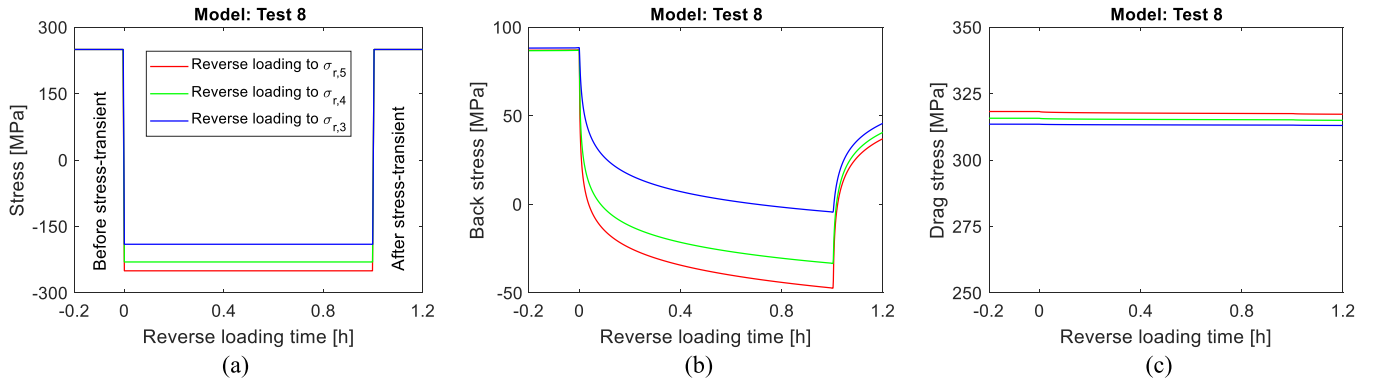


Fig. 10. Evolution of back stress (b) and drag stress (c) during reverse-loading to $\sigma_{r,3}$, $\sigma_{r,4}$ and $\sigma_{r,5}$ in segment 1 of test 8 (a).

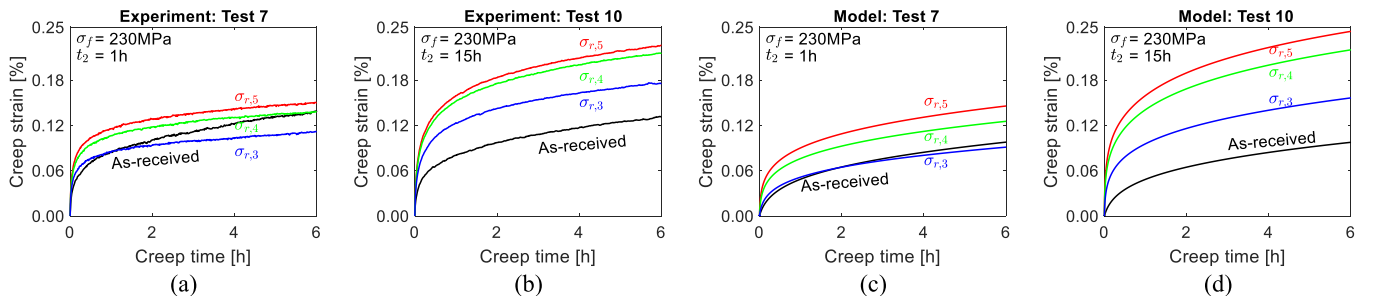


Fig. 11. Sensitivity of the PCR behaviour of the 10%Cr steel to the reverse-loading duration: experimental observations (a and b) and modelling results (c and d) for strain accumulation after 1 and 15 h reverse-loading to $\sigma_{r,3}$, $\sigma_{r,4}$ and $\sigma_{r,5}$ in segment 1 of tests 7 and 10.

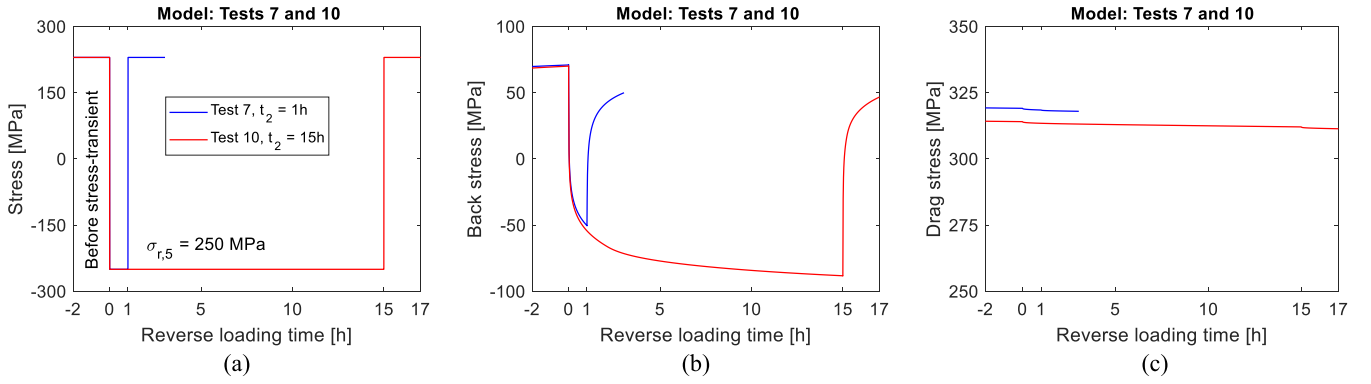


Fig. 12. Reverse-loading profile for different reverse-loading durations in segment 1 of tests 7 and 10 (a), and the corresponding back stress (b) and drag stress (c) evolutions.

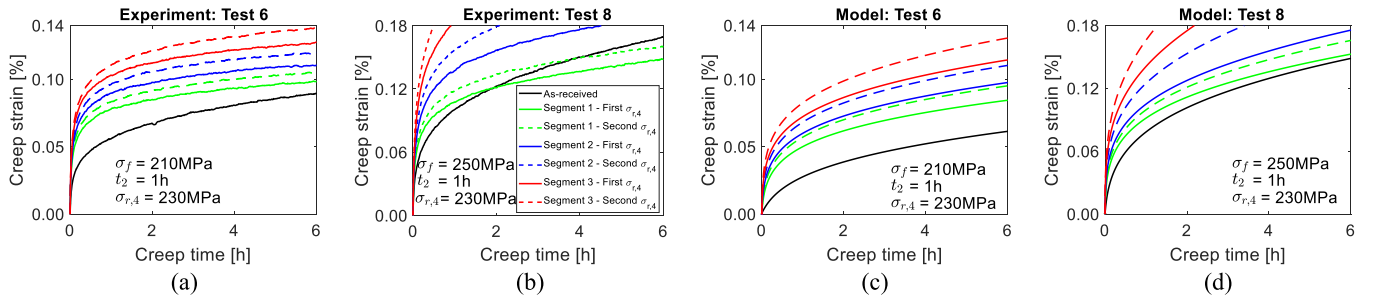


Fig. 13. Sensitivity of the PCR behaviour of the 10%Cr steel to the segment number: experimental observations (a and b) and modelling results (c and d) for strain accumulation after stress-transient to $\sigma_{r,4}$ for different segments of tests 6 and 8.

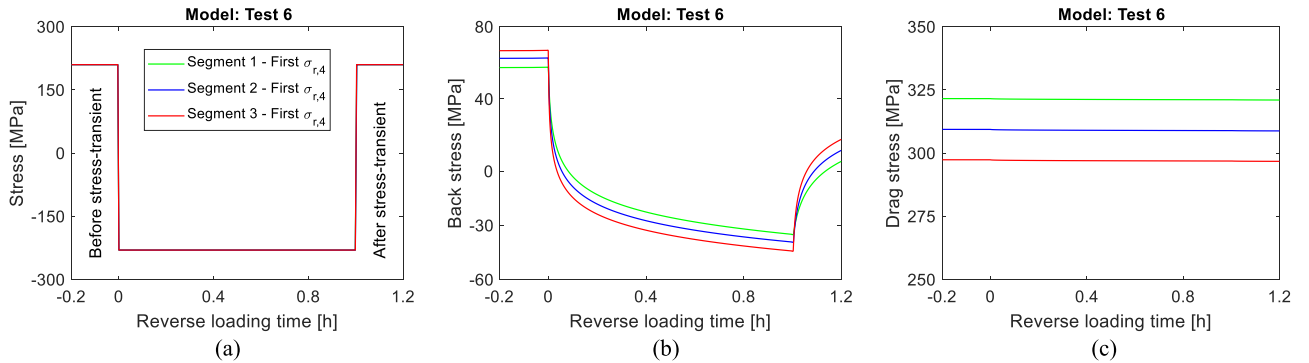


Fig. 14. Evolution of back stress (b) and drag stress (c) during reverse-loading to $\sigma_{r,4}$ for different segments of test 6 (a).

forward-stress level. According to Eq. (4), the smaller back stress results in a faster creep rate upon reloading and therefore more significant PCR. Fig. 16c indicates that drag stress evolution for the two presented conditions are similar and therefore it is expected that the drag stress plays an insignificant role in defining the PCR sensitivity to the forward-stress level.

4.2. Effect of stress-transients on the overall strain accumulation behaviour

Fig. 17 presents the experimental and model calculated strain accumulation behaviour of the 10% Cr steel under constant-load and stress-varying creep conditions (with different reverse-loading durations) for the forward-stress level of 230 MPa. It can be observed that for short reverse-loading durations ($t_2 = 0$ h and 1 h), multiple activations of PCR led to more significant overall strain accumulation and therefore the strain curves for these two test conditions (tests 3 and 7) are above the curve for the constant-load creep test. On the other hand, the large extent of compressive deformation during 15 h reverse-loading for test

10 affects the overall strain response and therefore the strain curve for this test is beneath the other curves.

Experimental observations for test 7 ($t_2 = 1$ h) and in particular for test 10 ($t_2 = 15$ h) indicate that the reverse-loading and subsequent PCR might accelerate the transition to the tertiary creep stage. For test 12 (constant-load), the material deformation is governed by secondary creep deformation at $t > 750$ h, while the stress-transients of test 10 lead to the early tertiary creep stage initiation already after $t < 650$ h. These observations highlight the importance of PCR consideration in the mechanical integrity assessment of high-temperature components operating under stress-varying (cyclic) creep loading conditions.

As presented in Fig. 17b, the predictions of the model for the effect of stress-transients on the overall strain accumulation behaviour of the alloy is fairly consistent with the experimental records. The developed model could consistently represent the acceleration of overall strain accumulation due to impose of stress-transients with $t_2 = 0$ and 1 h and also the drop of overall strain level due to 15 h reverse-loading periods. The model however does not include a damage formulation and there-

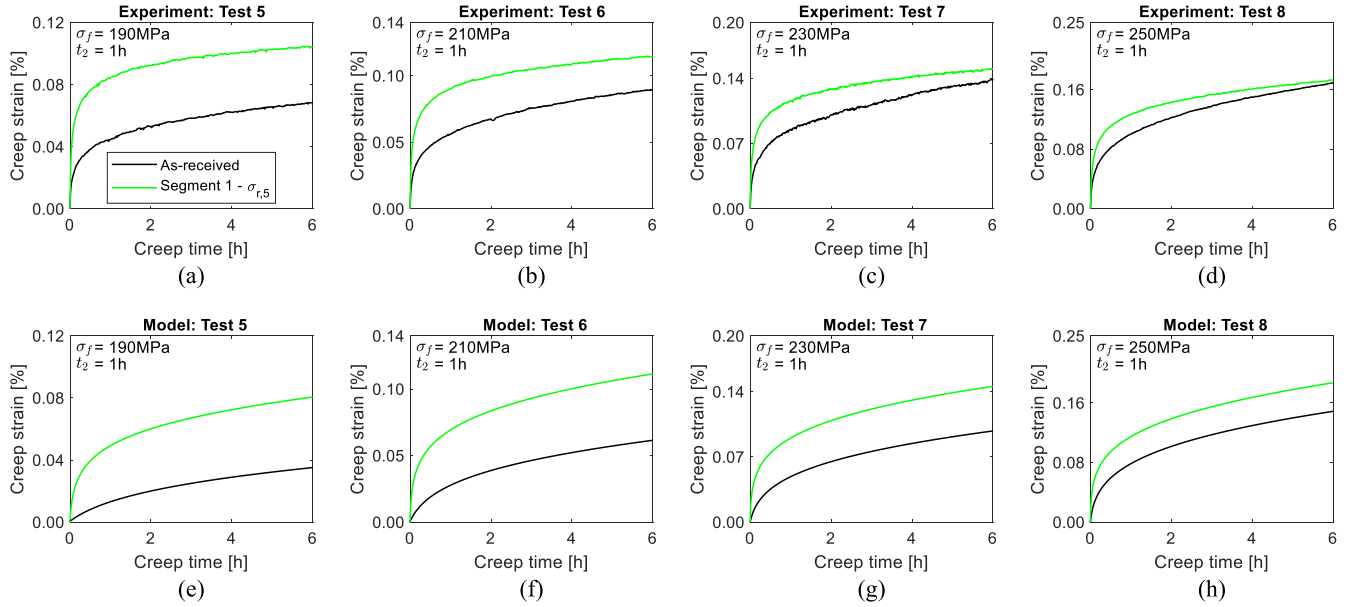


Fig. 15. Sensitivity of the PCR behaviour of the 10%Cr steel to the forward-stress level: experimental observations (a-d) and modelling results (e-h) for strain accumulation after stress-transients to $\sigma_{r,5}$ in segment 1 for tests with different forward-stress levels (tests 5–8). Experimental data are taken from [10].

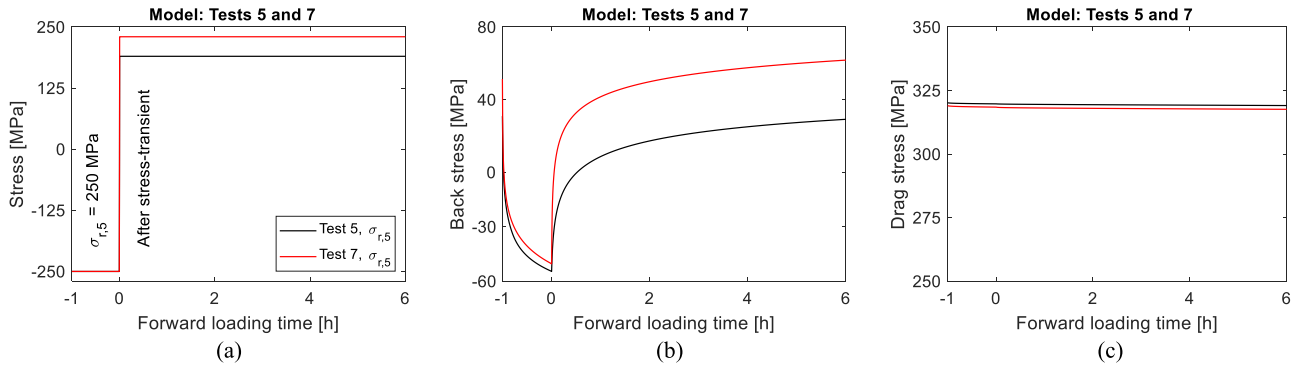


Fig. 16. Reverse-loading profile for different forward-stress levels in segment 1 of tests 5 and 7 (a), and the corresponding back stress evolution (b) and drag stress evolution (c).

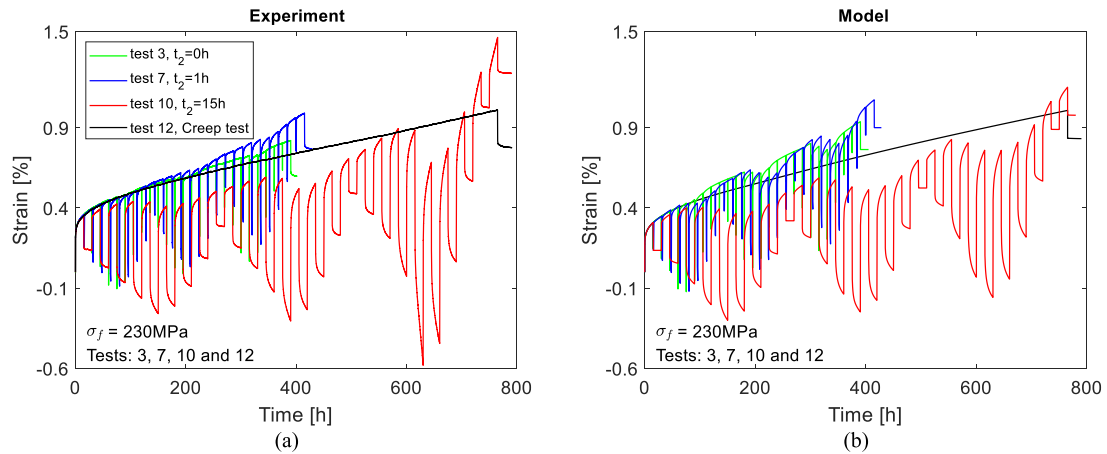


Fig. 17. Sensitivity of the overall strain accumulation behaviour of the 10%Cr steel to the introduction of stress-transients: experimental observations (a) and modelling results (b) for strain accumulation under the forward-stress level of 230 MPa with different reverse-loading durations for tests 3, 7, 10, and 12. Experimental data are taken from [10].

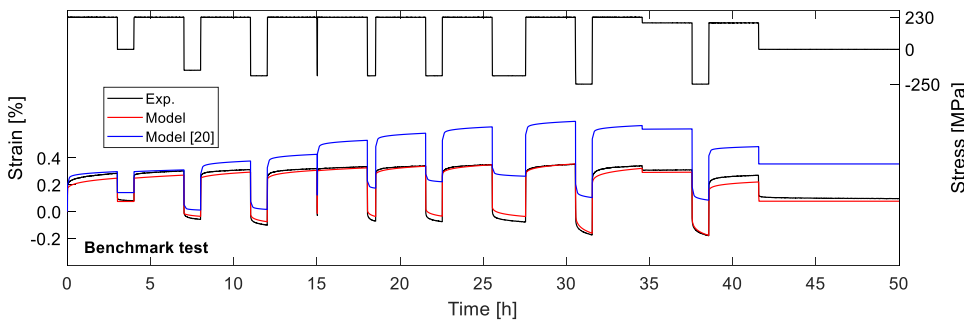


Fig. 18. Comparison of experimentally recorded and model-predicted strain accumulation behaviour of 10%Cr steel for the conducted benchmark test (models developed in the current study and in [20]).

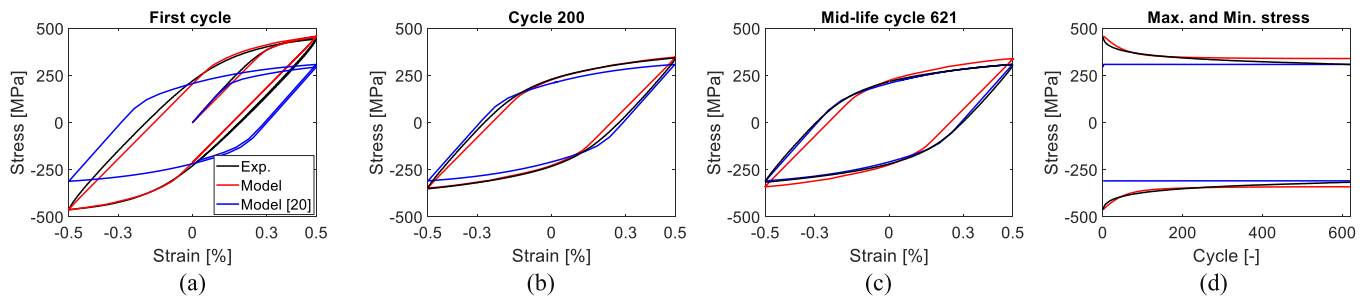


Fig. 19. Comparison of experimental and model-predicted stress-strain behaviour of 10%Cr steel during LCF loading (models developed in the current study and in [20]): first cycle (a), cycle 200 (b), mid-life cycle 621 (c) and evolution of maximum and minimum stresses in each cycle (up to mid-life cycle 621) (d). Experimental data are taken from [20].

fore is not able to capture the significant increase in the creep rate for test 10 at $t > 700$ h (i.e. tertiary creep stage).

4.3. Predictive capability examination

To evaluate its predictive capability, the developed model in this study has been employed for prediction of the behaviour of two independent benchmark tests. The experimental records from these two tests were not used in the calibration of the model. The benchmark tests include a (load-controlled) stress-varying creep test performed as a part of the present study (Fig. 2) and a strain-controlled low-cycle fatigue (LCF) test performed as a part of [20]. Furthermore, the material model introduced in [20] has also been used for prediction of the alloy response during the two benchmark tests.

Fig. 18 shows the comparison of experimental and model calculated strain profiles for the stress-varying benchmark creep test. It can be seen that the developed model in this study could well predict the strain evolution of the benchmark test, which had a rather complex stress profile in comparison with those for tests 1–10 (e.g. different forward-stress levels and different reverse-loading magnitudes and durations). The acceptable consistency between model predictions and experimental observations for the benchmark test demonstrates the effectiveness of the developed model for describing the creep behaviour of 10%Cr steel under complex loading conditions at 600 °C. On the other hand, the model developed in [20] failed to reliably predict the PCR phenomenon and often overestimated the creep strain rate after the stress transients.

Fig. 19 compares the predictions of the model with experimental observations for the 10%Cr steel at 600 °C subjected to strain-controlled LCF (strain range of $\pm 0.5\%$). The observations indicate that the developed model in this study could provide fairly reliable predictions for stress evolution up to the mid-life cycle (where fatigue damage development is negligible). Employment of the model for describing the cyclic stress-strain response of the alloy for larger fatigue life fractions requires the addition of a damage formulation. The developed model in [20] was originally developed for representing the steady-state or mid-life cycle response of the alloy and therefore provides experimentally consistent predictions for the midlife-cycle response of the alloy (Fig. 19c). How-

ever, it fails in predicting the deformation response of the alloy for the initial cycles.

5. Concluding remarks

An elastic-viscoplastic constitutive model for representing the creep behaviour of a 10%Cr steel at 600 °C under stress-varying loading condition has been developed. Similar to the different variants of the Chaboche viscoplastic model, isotropic and kinematic hardening/softening considerations, based on the back stress and drag stress quantities, are included in the model formulation. The effectiveness of the developed model to represent the primary creep regeneration (PCR) is examined, where PCR is the incidence of a period of high rate creep strain accumulation following a stress reversal. The model was employed for representing the experimental records from twelve dedicated stress-varying creep experiments which were designed for evaluating the PCR response of the alloy. It has been shown that the model can reliably represent the PCR phenomenon and describe its sensitivity to different loading conditions. Furthermore, the description of the model for the effect of imposed stress-transients on the overall creep strain accumulation behaviour of the steel were consistent with the experimental observations.

Ultimately and to examine its predictive capability, the developed model was employed for predicting the response of the alloy during two independent benchmark experiments; a load-controlled creep test with multiple stress-transients, and a strain-controlled low-cycle fatigue test. As the experimental data from the benchmark tests were not used for its calibration, the ability of the model to provide a fairly consistent representation of the experimental records demonstrated the predictive capability of the model.

Declaration of Competing Interest

The authors declare that they have no known competing financial interests or personal relationships that could have appeared to influence the work reported in this paper.

CRediT authorship contribution statement

X. Li: Conceptualization, Investigation, Methodology, Writing - original draft, Writing - review & editing. **S.R. Holdsworth:** Conceptualization, Supervision, Writing - review & editing. **E. Mazza:** Conceptualization, Supervision, Writing - review & editing. **E. Hosseini:** Conceptualization, Methodology, Supervision, Writing - original draft, Writing - review & editing.

Acknowledgements

Financial support by the **Swiss National Science Foundation (SNSF)**; grant number **169877** is gratefully acknowledged.

Supplementary materials

Supplementary material associated with this article can be found, in the online version, at [doi:10.1016/j.ijmecsci.2020.106044](https://doi.org/10.1016/j.ijmecsci.2020.106044).

References

- Li X, Holdsworth S, Mazza E, Hosseini E. Creep behaviour of AISI 316H stainless steel under stress-varying creep loading conditions: primary creep regeneration. *Mater High Temp* 2019;36(3):240–52.
- Jolliffe K. The flow of polycrystalline metals under simple shear. *Proc R Soc Lond A* 1952;213(1112):3–26.
- Andrade EdC, Jolliffe K. The flow of polycrystalline metals under simple shear. II.. *Proc R Soc Lond A* 1960;254(1278):291–316.
- Jolliffe K. The flow of polycrystalline metals under simple shear. III.. *Proc R Soc Lond A* 1963;271(1347):472–98.
- Carroll M, Serin K, Eggeler G. Anisotropic strain hardening following load reversal during high-temperature creep testing of superalloy single crystals. *Mater Sci Eng A* 2004;387:590–4.
- Sonnerup L. Stress reversals in connection with primary creep. Gumperts: Scandinavian University Books; 1965.
- Al Mamun A, Simpson C, Agius D, Lee TL, Kabra S, Truman C, Mostafavi M, Knowles D. A novel insight into the primary creep regeneration behaviour of a polycrystalline material at high-temperature using in-situ neutron diffraction. *Mater Sci Eng A* 2020;139374.
- Blass, J.J. and W.N. Findley, Short-time, biaxial creep of an aluminum alloy with abrupt changes of temperature and state of stress. 1971.
- Li X, Holdsworth S, Mazza E, Hosseini E. Comparison of primary creep regeneration and anelastic recovery behaviour of 316H austenitic and 10%Cr martensitic steel. *Mech Mater* 2020;103474.
- Li X, Holdsworth S, Mazza E, Hosseini E. Creep behaviour of a high chromium martensitic steel under stress varying creep loading conditions: primary creep regeneration (PCR). *Int J Press Vessels Piping* 2020;104188.
- Hosseini E, Holdsworth S, Mazza E. Advanced constitutive modelling for creep-fatigue assessment of high temperature components. *Mater High Temp* 2018;35(6):504–12.
- Spindler M. The prediction of creep damage in type 347 weld metal. Part I: the determination of material properties from creep and tensile tests. *Int J Press Vessels Piping* 2005;82(3):175–84.
- Spindler M. The prediction of creep damage in type 347 weld metal. Part II creep fatigue tests. *Int J Press Vessels Piping* 2005;82(3):185–94.
- Spindler M. An improved method to calculate the creep-fatigue endurance of type 316H stainless steel. 8th Liege conference on materials for advanced power engineering; 2006.
- Knowles D, Sheridan M, Montgomery O, Terry N. Creep-fatigue life assessment of reheater tubes at detuning strap connections. *Atkins Tech J* 2020;41–8 Paper 086 - Energy. <https://www.atkinsglobal.com/~media/Files/A/Atkins-Global/Attachments/sectors/power/library-docs/technical-papers/creep-fatigue-life-assessment-of-reheater.pdf>.
- Petkov MP, Hu J, Cocks AC. Self-consistent modelling of cyclic loading and relaxation in austenitic 316H stainless steel. *Philos Mag* 2019;99(7):789–834.
- Radosavljevic M. Creep-fatigue assessment of high temperature steam turbine rotors (Diss ETH No. 19880) PhD thesis. ETHZ University; 2011.
- Chaboche J-L. A review of some plasticity and viscoplasticity constitutive theories. *Int J Plast* 2008;24(10):1642–93.
- Metzger M, Seifert T. On the exploitation of Armstrong-Frederik type nonlinear kinematic hardening in the numerical integration and finite-element implementation of pressure dependent plasticity models. *Comput Mech* 2013;52(3):515–24.
- Hosseini E, Holdsworth S, Kühn I, Mazza E. Temperature dependent representation for Chaboche kinematic hardening model. *Mater High Temp* 2015;32(4):404–12.
- Hosseini E, Holdsworth S, Kühn I, Mazza E. Modelling heat-to-heat variability in high temperature cyclic deformation behaviour. *Mater High Temp* 2015;32(3):347–54.
- Benaarbia A, Rae Y, Sun W. Unified viscoplasticity modelling and its application to fatigue-creep behaviour of gas turbine rotor. *Int J Mech Sci* 2018;136:36–49.
- Krausz AS, Krausz K. Unified constitutive laws of plastic deformation. Elsevier; 1996.
- Walker, K.P., Research and development program for non-linear structural modeling with advanced time-temperature dependent constitutive relationships. 1981.
- Chen W, Wang F, Kitamura T, Feng M. A modified unified viscoplasticity model considering time-dependent kinematic hardening for stress relaxation with effect of loading history. *Int J Mech Sci* 2017;133:883–92.
- Kyaw ST, Rouse JP, Lu J, Sun W. Determination of material parameters for a unified viscoplasticity-damage model for a P91 power plant steel. *Int J Mech Sci* 2016;115:168–79.
- Chaboche J, Nouailhas D. A unified constitutive model for cyclic viscoplasticity and its applications to various stainless steels. *J Eng Mater Technol* 1989;111(4):424–30.
- Saad A, Hyde CJ, Sun W, Hyde T. Thermal-mechanical fatigue simulation of a P91 steel in a temperature range of 400–600 °C. *Mater High Temp* 2011;28(3):212–18.
- Saad AA, Hyde T, Sun W, Hyde CJ, Tanner DW. Characterization of viscoplasticity behaviour of P91 and P92 power plant steels. *Int J Press Vessels Piping* 2013;111:246–52.
- Li D-H, Shang D-G, Li Z-G, Wang J-J, Hui J, Liu X-D, Tao Z-Q, Zhang C-C, Chen B. Unified viscoplastic constitutive model under axial-torsional thermo-mechanical cyclic loading. *Int J Mech Sci* 2019;150:90–102.
- Barrett RA, O'Hara EM, O'Donoghue PE, Leen SB. High-temperature low-cycle fatigue behavior of MarBN at 600 °C. *J Press Vessel Technol* 2016;138(4):041401.
- Hyde CJ, Sun W, Leen SB. Cyclic thermo-mechanical material modelling and testing of 316 stainless steel. *Int J Press Vessels Piping* 2010;87(6):365–72.
- Barrett R, Farragher T, Hyde CJ, O'Dowd N, O'Donoghue P, Leen SB. A unified viscoplastic model for high temperature low cycle fatigue of service-aged P91 steel. *J Press Vessel Technol* 2014;136(2):021402.
- Hosseini E, Kazemi A, Abrinia K, Shahsavari H, Holdsworth S, Baghani M. Effect of prior deformation on the subsequent creep and anelastic recovery behaviour of an advanced martensitic steel: unified constitutive modelling. *Int J Mech Sci* 2020;176:105546.
- Zang S, Guo C, Thuillier S, Lee M. A model of one-surface cyclic plasticity and its application to springback prediction. *Int J Mech Sci* 2011;53(6):425–35.
- Paul SK, Sivaprasad S, Dhar S, Tarafder M, Tarafder S. Simulation of cyclic plastic deformation response in SA333 C–Mn steel by a kinematic hardening model. *Comput Mater Sci* 2010;48(3):662–71.
- Shojaei A, Eslami M, Mahbadi H. Cyclic loading of beams based on the Chaboche model. *Int J Mech Mater Des* 2010;6(3):217–28.
- Kumar P, Singh A. Investigation of fracture behaviour and low cycle fatigue properties of cryorolled Al-Mg alloy. *Theor Appl Fract Mech* 2018;98:78–94.
- Shrestha T, Basirat M, Charit I, Potirniche GP, Rink KK, Sahaym U. Creep deformation mechanisms in modified 9Cr–1Mo steel. *J Nucl Mater* 2012;423(1–3):110–19.
- Langdon TG. Identifying creep mechanisms at low stresses. *Mater Sci Eng A* 2000;283(1–2):266–73.
- Naumenko K, Altenbach H, Gorash Y. Creep analysis with a stress range dependent constitutive model. *Arch Appl Mech* 2009;79(6–7):619–30.
- Naumenko K, Gariboldi E, Nizinkovskiy R. Stress-regime-dependence of inelastic anisotropy in forged age-hardening aluminium alloys at elevated temperature: constitutive modeling, identification and validation. *Mech Mater* 2020;141:103262.
- Hosseini E, Holdsworth S, Mazza E. Experience with using the LICON methodology for predicting long term creep behaviour in materials. *Int J Press Vessels Piping* 2012;92:70–6.
- Zhang J, Wang G, Xuan F, Tu S. The influence of stress-regime dependent creep model and ductility in the prediction of creep crack growth rate in Cr–Mo–V steel. *Mater Des* (1980–2015) 2015;65:644–51.
- Hu J, Chen B, Smith DJ, Flewitt PE, Cocks AC. On the evaluation of the Bauschinger effect in an austenitic stainless steel—the role of multi-scale residual stresses. *Int J Plast* 2016;84:203–23.
- Petkov MP, Hu J, Tarleton E, Cocks AC. Comparison of self-consistent and crystal plasticity FE approaches for modelling the high-temperature deformation of 316H austenitic stainless steel. *Int J Solids Struct* 2019;171:54–80.
- Chaboche J-L. Elasto-viscoplasticity, 16. Athens: Nonlinear Computational Mechanics; 2009. p. 2009.
- Metzger M, Knappe M, Seifert T. Models for lifetime estimation of cast iron components. *MTZ worldwide eMagazine* 2011;72(10):70–7.
- Seifert T, Riedel H. Mechanism-based thermomechanical fatigue life prediction of cast iron. Part I: Models. *Int J Fatigue* 2010;32(8):1358–67.